Predicting the dynamic behavior of the mechanical properties of platinum with machine learning

James Chapman and Rampi Ramprasad

View Online   **Export Citation**   **CrossMark**

ARTICLES YOU MAY BE INTERESTED IN

Predicting the dynamic behavior of the mechanical properties of platinum with machine learning

View Online   Export Citation   CrossMark

James Chapman (ID) and Rampi Ramprasad[a)]

AFFILIATIONS

Department of Materials Science and Engineering, Georgia Institute of Technology, Atlanta, Georgia 30332, USA

Note: This paper is part of the JCP Special Topic on Machine Learning Meets Chemical Physics.
[a)]Author to whom correspondence should be addressed: rampi.ramprasad@mse.gatech.edu. **Also at:** Department of Materials Science and Engineering, Georgia Institute of Technology, Atlanta, Georgia 30332, USA.

ABSTRACT

Over the last few decades, computational tools have been instrumental in understanding the behavior of materials at the nano-meter length scale. Until recently, these tools have been dominated by two levels of theory: quantum mechanics (QM) based methods and semi-empirical/classical methods. The former are time-intensive but accurate and versatile, while the latter methods are fast but are significantly limited in veracity, versatility, and transferability. Recently, machine learning (ML) methods have shown the potential to bridge the gap between these two chasms due to their (i) low cost, (ii) accuracy, (iii) transferability, and (iv) ability to be iteratively improved. In this work, we further extend the scope of ML for atomistic simulations by capturing the temperature dependence of the mechanical and structural properties of bulk platinum through molecular dynamics simulations. We compare our results directly with experiments, showcasing that ML methods can be used to accurately capture large-scale materials phenomena that are out of reach of QM calculations. We also compare our predictions with those of a reliable embedded atom method potential. We conclude this work by discussing how ML methods can be used to push the boundaries of nano-scale materials research by bridging the gap between QM and experimental methods.

Published under license by AIP Publishing. https://doi.org/10.1063/5.0008955

I. INTRODUCTION

Atomistic computational techniques have been used to examine a plethora of nano-scale materials phenomena.[1-6] These methods have generally fallen into two broad categories: quantum mechanics (QM) based methods, e.g., density functional theory (DFT),[7,8] and semi-empirical methods, e.g., the embedded atom method (EAM).[9-15] While both classes have been widely used to accurately study materials under a range of conditions,[16-19] they both suffer from serious drawbacks. QM methods, while able to provide access to properties at an extremely high level of fidelity, are computationally cumbersome and severely restrict both the time and length scales that can be studied. Semi-empirical methods, however, fill this void by significantly reducing the computational cost and allow for

the exploration of both large systems and long simulation times. However, the trade-off is accurate, as such methods are generally fit to specific regions of a material's configuration space and are often not generalizable.[20]

To this end, data-driven machine learning (ML) methods have demonstrated their ability to be a reliable alternative, bridging the gap in cost, accuracy, and transferability.[21-29] Unlike the previously mentioned classes of computational techniques, ML methods rely on functional forms that are statistically derived, rather than physically derived. Such models will still suffer when extrapolating and will generally fail more quickly than their semi-empirical counterparts. However, ML approaches offer a number of advantages over these methods such as the time required to construct a new model, their accuracy when compared to QM methods, and their ability to

be iteratively improved in a systematic manner.[1,30–38] ML methods are also opening up avenues for accelerating discovery of materials, in general.[25,29,39–42]

Throughout the last half-century, numerous experimental studies for platinum have provided a robust understanding of how the mechanical properties of platinum are affected by the changes in temperature.[43–47] However, recent work using several embedded atom method (EAM) based classical potentials has shown that all studied models cannot reliably predict this behavior.[2] QM methods have also struggled to reliably capture such phenomena due to the time and length scales required to accurately study them.[48,49] Furthermore, we recently demonstrated the capability of the AGNI platform to accurately predict the mechanical properties of platinum at 0 K.[38]

In this letter, we demonstrate the use of these recent AGNI models in exploring how the mechanical properties of platinum are affected by the changes in temperature. In particular, we utilize molecular dynamic (MD) simulations, coupled with varying forms of strain, to predict the dynamic behavior of elastic constants. Mechanical properties, such as the bulk, shear, and Young's modulus, can then be predicted using the Voigt–Reuss–Hill approximation.[50] The remainder of this letter is as follows: We first begin by providing the reader with a brief overview of the AGNI methodology. Second, we discuss the dynamic behavior of the elastic constants of platinum, and from them, the bulk, shear, and Young's modulus. Finally, we discuss the temperature dependence of several other properties, such as the coefficient of thermal expansion, lattice parameter, and isothermal compressibility. The compilation of atomistic phenomena presented in this work aims to further push the boundaries of ML methods for simulations of dynamic materials by bridging the gap between QM, semi-empirical, and experimental methodologies.

II. COMPUTATIONAL DETAILS

A. AGNI workflow

The AGNI platform consists of several key steps, regardless of the property being predicted: (1) the generation of a diverse set of reference data, (2) numerically encoding local/structural geometric information (fingerprinting), (3) training a ML model, given some subset of the reference data, and (4) employing the final ML models in an MD engine, capable of simulating the dynamic, time-evolution of atomistic processes. Throughout sections B, C, and D we will provide a brief explanation of steps (1), (2), and (3), respectively, and we refer the reader to our previous works for a more thorough understanding.[30–32,37,38,51]

B. Reference data generation

A comprehensive set of reference data, summarized in Table I, was prepared for Pt in an accurate and uniform manner in order to minimize numerical noise intrinsic to atomistic calculations. All reference data were obtained using the Vienna *Ab initio* simulation package (VASP).[52–56] The Perdew–Burke–Ernzerhof (PBE) functional[57] was used to calculate the electronic exchange–correlation interaction. Projector augmented wave (PAW) potentials[58] and plane-wave basis functions up to a kinetic energy cutoff of 500 eV

TABLE I. Summary of the reference dataset that was prepared for platinum force field generation. The data are divided into subsets based on the type of defect that is present. T = 0 K represents NEB calculations, where T > 0 K represents MD calculations. Configurations are represented by each atomic configuration present in the data. For the system containing four vacancies, the vacancy configurations represent two isolated vacancies and one divacancy in a 108-atom cell (104 total atoms).

Defect type	Systems	Temperature (K)
Defect-free	Bulk (w/o strain)	300, 1000, 2000
Defect-free	Bulk (w/strain ± 7%)	300, 1000, 2000
Point defect	Bulk with 1 vacancy	0, 1000, 1500, 2000
Point defect	Bulk with divacancy	0, 1000, 1500, 2000
Point defect	Bulk with 4 vacancies	1000, 1500, 2000

were used. All projection operators (involved in the calculation of the non-local part of the PAW pseudopotentials) were evaluated in the reciprocal space to ensure further precision. Monkhorst–Pack[59] **k**-point meshes were carefully calibrated for each atomic configuration to ensure numerical convergence in both energy and atomic forces. For all nudged elastic band (NEB) calculations, the climbing image formalism was employed[56] with ionic relaxations considered converged at an energy difference of 10^{-2} eV and electronic convergence terminated at an energy difference of 10^{-4} eV.

C. Fingerprinting atomic configurations

A stratified representation of an atom's local structural environment was created to capture geometric information that is mapped directly to properties such as the total potential energy, atomic forces, and stresses. This hierarchy aims to capture unique aspects of the atomic neighborhood with features resembling scalar, vector, and tensor quantities. The functional forms of all atomic-level fingerprint components are defined as[51,60]

$$S_{i;k} = c_k \sum_{j \neq i} \exp\left[-\frac{1}{2}\left(\frac{r_{ij}}{\sigma_k}\right)^2\right] f_{cut}(r_{ij}), \qquad (1)$$

$$V_{i,\alpha;k} = c_k \sum_{j \neq i} \frac{r_{ij}^{\alpha}}{r_{ij}} \exp\left[-\frac{1}{2}\left(\frac{r_{ij}}{\sigma_k}\right)^2\right] f_{cut}(r_{ij}), \qquad (2)$$

$$T_{i,\{\alpha,\beta\};k} = c_k \sum_{j \neq i} \frac{r_{ij}^{\alpha} r_{ij}^{\beta}}{r_{ij}^2} \exp\left[-\frac{1}{2}\left(\frac{r_{ij}}{\sigma_k}\right)^2\right] f_{cut}(r_{ij}), \qquad (3)$$

with r_i and r_j being the Cartesian coordinates of atoms i and j and $r_{ij} = |\mathbf{r}_j - \mathbf{r}_i|$. α and β represent any of the three x, y, or z directions. The σ_k values control the width of the Gaussian functions and are determined via a grid-based optimization process.[32] The damping function $f_{cut}(r_{ij}) = \frac{1}{2}\left[\cos\left(\frac{\pi r_{ij}}{R_{cut}}\right) + 1\right]$ smoothly decays toward zero and has a cut-off radius R_{cut} chosen to be 8 Å. c_k is a normalization constant given by $\left(\frac{1}{\sigma_k \sqrt{2\pi}}\right)^3$ (for the force model, this normalization constant was set to 1).

In order to learn rotationally invariant properties, such as the total potential energy, a separate step is required to map the atomic fingerprints to rotationally invariant structural fingerprints. This

process involves mapping the atomic fingerprints described above to a single structural fingerprint, which is defined as[38,51]

$$V_{i,k} = \sqrt{(V_{i,x;k})^2 + (V_{i,y;k})^2 + (V_{i,z;k})^2},\tag{4}$$

$$
\begin{aligned}
T'_{i,k} &= T_{i,\{x,x\},k} T_{i,\{y,y\},k} + T_{i,\{x,x\},k} T_{i,\{z,z\},k} \\
&+ T_{i,\{y,y\},k} T_{i,\{z,z\},k} - \left(T_{i,\{x,y\},k}\right)^2 - \left(T_{i,\{x,z\},k}\right)^2 \\
&- \left(T_{i,\{y,z\},k}\right)^2,
\end{aligned}\tag{5}
$$

and

$$T''_{i,k} = det\left(T_{i,\{\alpha,\beta\},k}\right).\tag{6}$$

In this work, ML models that learn the potential energy employ such a procedure. Table II indicates the final forms of all fingerprints for energy, stresses, and forces. Here, the function $M^n(X)$ represents the nth moment of the fingerprint components. For this work, only the first ($n = 1$) moment is considered and can be interpreted as the average atomic environment of the system.

D. Machine learning

After the final fingerprint forms have been established and a subset of our reference data has been selected, we turn to Kernel Ridge Regression (KRR) to create ML models for atomic forces, potential energy, and the stress tensor. This learning scheme employs a similarity-based non-linear functional form to create a mapping between the reference fingerprints and the desired property using a form described as[1,30–33,38]

$$P_X = \sum_Y \alpha_Y \exp\left[-\frac{1}{2}\left(\frac{d_{XY}}{\sigma}\right)^2\right].\tag{7}$$

Here, the summation runs over the number of reference environments Y in a model's training set. P symbolizes the desired property (total potential energy, stress tensor components, or atomic forces), with X being the fingerprint of the structure whose properties are being predicted. d_{XY} represents the L^2 norm between fingerprints X and Y, calculated within the fingerprint hyperspace, and is specified by a length scale σ. During the model's training phase, the regression weights α_Y and the length scale σ are determined via a regularized objective function, which is optimized through a 5-fold

cross validation process. At the end of the model generation process, there will be three independent ML models for energy, forces, and stresses. Statistical metrics, used to compare the ML model's predictions with all reference data used in this work, can be found in Table III.

E. Simulations details

MD simulations were used to capture both the tensile and shear strains of single crystal fcc platinum using the Large-scale Atomic/Molecular Massively Parallel Simulator (LAMMPS) package.[61] This ML scheme has been bench-marked against both EAM and DFT, for the calculation of energy, forces, and stresses, and is approximately 5 orders of magnitude faster than DFT, but roughly 2 orders of magnitude slower than EAM. Simulations were performed for a temperature range of 100 K–1000 K. Temperatures above 1000 K were not considered as reliable experimental values do not exist in this regime. Simulations at temperatures lower than 100 K were also not considered in this work as it has been shown that zero-point energy contributions become non-negligible below 100 K for platinum.[62,63] As the simulations considered in this work are classical in nature and do not consider quantum effects, temperatures below 100 K cannot be reliably predicted.

For the case of tensile strain, a $21 \times 21 \times 21$ supercell containing 37 044 atoms is used. NPT simulations, run for 2 ns at $P = 0$, are used to equilibrate the supercell volume at a given temperature. Then, NVT simulations are performed, in which the cell was strained along the X axis at a rate of $10^{-3}\frac{1}{ps}$ for 10 ns. As the strain along the Y and Z axis remains constant at 0, the elastic constants can be calculated from the stress–strain relationships defined by $\sigma_{xx} = C_{11}e_{xx} + C_{12}(e_{yy} + e_{zz})$ and $\sigma_{yy} = C_{11}e_{yy} + C_{12}(e_{xx} + e_{zz})$, where C_{ij} is a given elastic constant, σ_{ii} is the stress along the ii direction, and e_{ii} is the strain along the ii direction.

For the case of shear strain, the same supercell and simulation arrangement employed during the tensile strain test was used. However, due to the stress–strain relationship, defined by $\sigma_{xy} = C_{44}e_{xy}$, the initial supercell was defined with tilt factors, initially set to 0. After an equilibration run, as defined previously, the cell was deformed along both the X and Y axis, uniformly, at a rate of $10^{-3}\frac{1}{ps}$ for 10 ns. For both tensile and shear strains, the stress was plotted against the strain for a given elastic constant. A linear regression curve was then fit to the stress–strain relationship,

TABLE II. The final fingerprint forms utilized to learn energy, stresses, or atomic forces. For the property type, the subscripts i and I represent a per-atom or per-structure quantity, respectively, and the superscripts α, β represent two possible Cartesian directions.

Property type	No. of σ_k	σ_k range (Å)	Final fingerprint form
Forces (F_i^α)	8	(1.0, 9.0)	$V_{i,\alpha;k}$
Stresses ($S_I^{\alpha,\beta}$)	20	(1.5, 11.5)	$M^n\left(\sum_{i=1}^N T_{i,\{\alpha,\beta\};k}\right)$
Energy (E_I)	20	(1.5, 11.5)	$\left\{M^n\left(\sum_{i=1}^N S_{i,k}\right), M^n\left(\sum_{i=1}^N V_{i,k}\right), M^n\left(\sum_{i=1}^N T_{i,k}\right)\right\}$

TABLE III. Statistical error metrics of the final ML models, for each property learned, generated in this work. All values presented here are the metrics calculated on a given model's test set. The final row corresponds to the number of training points in the final models chosen for this work.

Error metric	Energy model (meV/atom)	Force model (eV/Å)	Stress model (GPa)
RMSE	2.73	0.15	0.42
STD	2.71	0.15	0.41
Max 1% error	7.90	0.80	1.68
r^2	0.99	0.99	0.99
No. of training points	1728	3000	3000

whose slope is the corresponding elastic constant. An R^2 fit of 0.95, as a minimum, was used to determine a line's convergence before extracting the elastic constants. The bulk, shear, and Young's modulus were then calculated from the predicted elastic constants using the Voigt–Reuss–Hill approximation.[50]

MD simulations were also performed for properties such as the coefficient of linear expansion and the change in lattice parameter as a function of temperature. A $25 \times 25 \times 25$ supercell, containing 62 500 atoms, was used. NPT simulations, run for 10 ns, were performed for temperatures between 100 K and 2000 K. The final lattice parameter was carefully chosen only after a strict convergence criterion of 10^{-3} Å was met. For the calculation of the coefficient of linear expansion, the reference temperature was set at 300 K to compare with experimental values.

III. RESULTS AND DISCUSSION

The dynamic, temperature dependent behavior of the mechanical properties of platinum was calculated via MD simulations. Figure 1 shows the change in the C_{11}, C_{12}, and C_{44} elastic constants as the temperature is increased from 100 K to 1000 K. Three sets

of values are shown: (1) experimental values,[2,64] (2) AGNI predictions, and (3) EAM predictions. The EAM values shown in Fig. 1 were taken from previous studies.[2] While several EAM potentials were studied in previous works, only the most reliable potential values are shown here. This EAM potential will henceforth be referred to as EAM-A due to its primary author James Adams.

One important point that must be mentioned is the relative vs absolute nature of the properties discussed in the remainder of this article. As both ML and semi-empirical potentials are fit to a set of reference data, one cannot always compare the absolute values of a predicted property to experimental values. For example, as shown in our previous work,[1,38] the absolute value of the 0 K elastic constants will deviate significantly from experiments at low temperature. This discrepancy, however, is not due to the model's failure, but rather the value that the model's reference level of theory predicts. In this case, the AGNI models are trained on the reference DFT data, generated using the PBE exchange–correlation functional, which deviate from experiments significantly.[38,65,66] Therefore, AGNI cannot be expected to predict absolute property values equivalent to experiments but will make predictions at the corresponding DFT level of theory. Due to these differences among various levels of theory, one
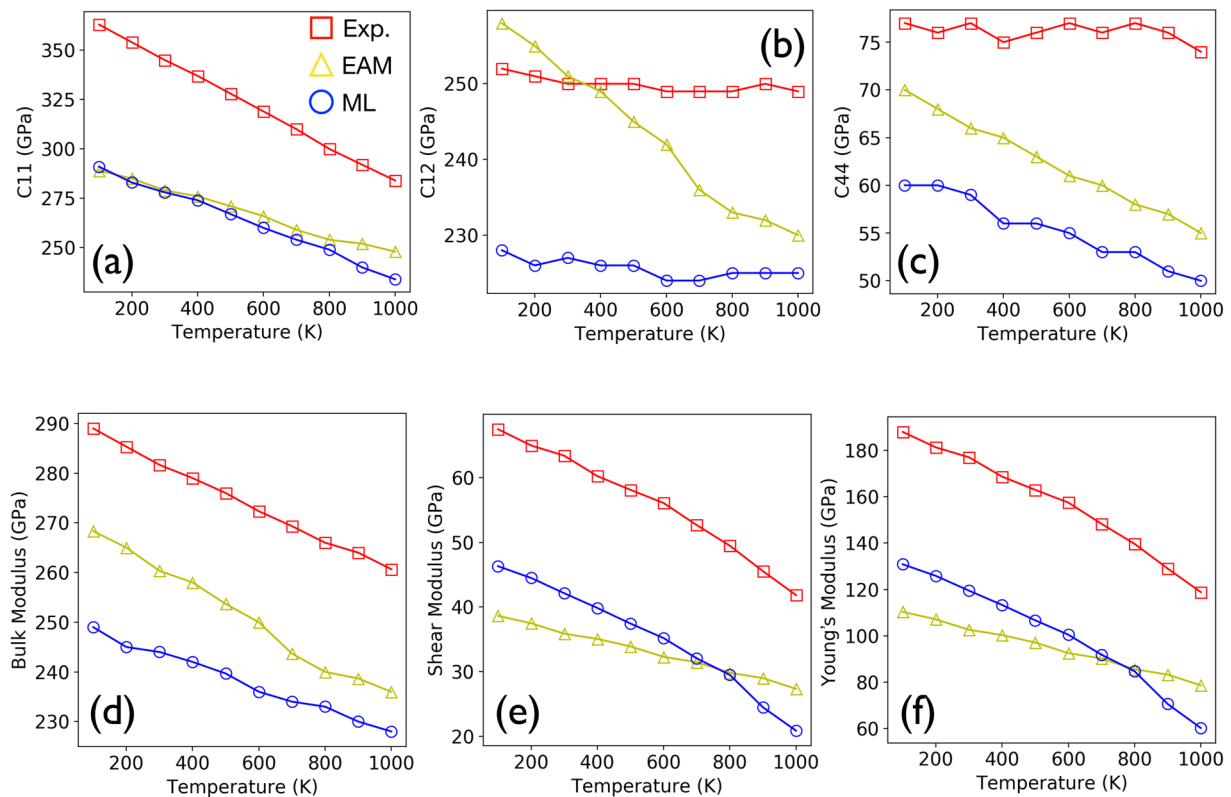
FIG. 1. (Top) The elastic constants C_{11}, C_{12}, and C_{44}, (a)–(c), respectively, for our AGNI models (blue), an EAM potential (yellow), and experiments (red) are shown. While absolute values between computational methods and experiments will rarely agree explicitly, due to deviations between experiments and the reference data used to fit the computational models, the difference in slopes should be negligible in order to be considered in agreement with experiments. The AGNI models are the only computational method whose slopes agree quantitatively with experiments. (Bottom) The bulk, shear, and Young's modulus, (d)–(f), respectively, is shown for our AGNI models (blue), an EAM potential (yellow), and experiments (red). These values were calculated using the elastic constants using the Voigt–Reuss–Hill approximation.[50]

TABLE IV. Absolute values for the properties predicted in this work. δ represents the percent difference between the property values at 100 K vs 1000 K. $\frac{dX}{dT}$ represents the slope of a given property as a function of temperature.

| Property	Experiments	EAM-A	AGNI
$\delta C_{11}(\%)$	22	14	20
$\delta C_{12}(\%)$	1	11	1
$\delta C_{44}(\%)$	4	21	16
$\delta B(\%)$	10	12	8
$\frac{dB}{dT}\left(\frac{\text{GPa}}{\text{K}}\right)$	-0.03	-0.04	-0.02
$\delta\mu(\%)$	39	29	54
$\frac{d\mu}{dT}\left(\frac{\text{GPa}}{\text{K}}\right)$	-0.03	-0.01	-0.03
$\delta E(\%)$	37	29	53
$\frac{dE}{dT}\left(\frac{\text{GPa}}{\text{K}}\right)$	-0.07	-0.03	-0.07
$\frac{d\beta}{dT}\left(\frac{1}{\text{GPa K}}\right)$	4.17×10^{-7}	5.67×10^{-7}	4.11×10^{-7}
$\frac{da}{dT}\left(\frac{\text{Å}}{\text{K}}\right)$	9.33×10^{-5}	...	1.16×10^{-4}

cannot rely on absolute values but rather on the quantitative and qualitative trends that the models yield with respect to experiments.

With this in mind, we begin by looking at several important trends that can be observed from the C_{11}, C_{12}, and C_{44} elastic constants as the temperature is increased from 100 K to 1000 K. Figure 1 shows a visual manifestation of these trends, while Table IV provides the absolute values. Experimentally, C_{11} has been shown to decrease by ~22% between 100 K and 1000 K, while EAM-A predicts a thermal degradation of (14%), and the AGNI framework predicts a degradation of (20%). Contrary to C_{11}, however, both C_{12}, and C_{44} show little to no thermal degradation experimentally, (1%) and (4%), respectively. However, EAM-A shows significant thermal degradation with respect to experiments in both C_{12} (11%) and C_{44} (21%). The AGNI framework performs substantially better than EAM-A, yielding degradation of (1%) and (16%) for C_{12}, and C_{44}, respectively. While AGNI's predicted change in C_{11} and C_{12} between is nearly identical when compared to experiments, thermal degradation in C_{44} is still four times that of experiments, although EAM-A yields a degradation greater than five times that of experiments.

Understanding how a material will respond to various forms of stress is critically important for a variety of applications.[2,67–69] To this end, the dynamic behavior of the bulk, shear, and Young's modulus can be calculated from the predicted elastic constants using the Voigt–Reuss–Hill approximation.[50] Figure 1 and Table IV show the change in these properties as the temperature is increased from 100 K to 1000 K. Experimental predictions of the bulk modulus indicate a thermal degradation of (10%), compared to a degradation of (12%) and (8%) for EAM-A and AGNI, respectively. Therefore, one can argue that both EAM and AGNI will perform equally well in understanding the resistance to compression. For the shear modulus, experimental values indicate a thermal loss of (39%), compared to a degradation of (29%) and (54%) for EAM-A and AGNI, respectively. Finally, for Young's modulus, experimental values indicate a decrease of (37%), compared to a decrease of (29%) and (53%) for EAM-A and AGNI, respectively. From these metrics, both AGNI and EAM show moderate deviations, when compared to experiments, when understanding the response to both linear and shear stresses.

However, if we assume that the change in these properties is perfectly linear between 100 K and 1000 K, we can easily calculate their slopes, shown in Table IV, which will provide the rate in which these properties change as a function of temperature. For the case of the bulk modulus, we arrive at slopes of $-0.03\frac{\text{GPa}}{\text{K}}$, $-0.04\frac{\text{GPa}}{\text{K}}$, and $-0.02\frac{\text{GPa}}{\text{K}}$ for experiments, EAM-A, and AGNI, respectively. For the shear modulus, we obtain slopes of $-0.03\frac{\text{GPa}}{\text{K}}$, $-0.01\frac{\text{GPa}}{\text{K}}$, and $-0.03\frac{\text{GPa}}{\text{K}}$ for experiments, EAM-A, and AGNI, respectively. Finally, for Young's modulus, we calculate slopes of $-0.07\frac{\text{GPa}}{\text{K}}$, $-0.03\frac{\text{GPa}}{\text{K}}$, and $-0.07\frac{\text{GPa}}{\text{K}}$ for experiments, EAM-A, and AGNI, respectively. Therefore, while EAM-A and AGNI's prediction yields moderate errors when one considers only the absolute thermal degradation over the entire temperature range, the slopes of these relationships tell a different story, where AGNI outperforms EAM-A significantly.

Another important aspect of the dynamic mechanical response of platinum that must be well understood is the physical change in the supercell as a function of temperature. To this end, we present calculations for the lattice parameter, coefficient of isothermal compressibility, and coefficient of linear expansion, shown in Fig. 2 and
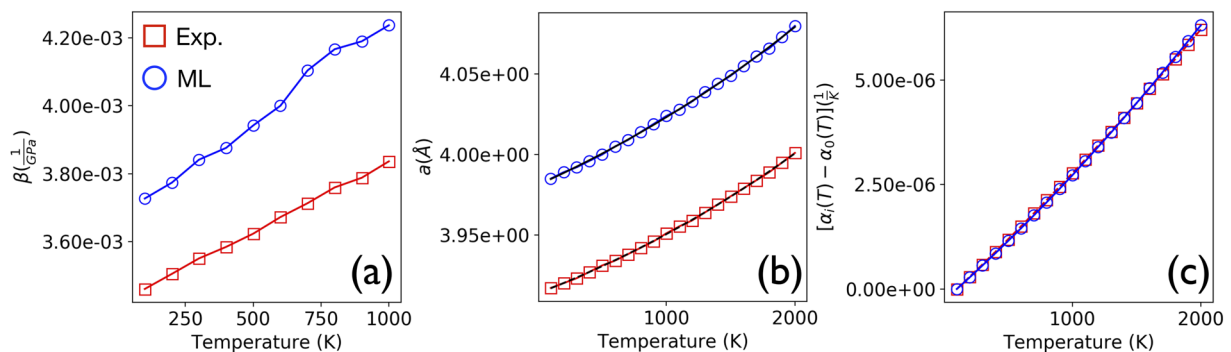
FIG. 2. The coefficient of isothermal compressibility, change in lattice parameter, and coefficient of linear expansion, (a)–(c) respectively, are shown for our AGNI models (blue) and experiments (red). Lattice parameter values (b) are used to fit a cubic spline (shown in black). Linear expansion values (c) are then calculated from the derivative of the cubic spline.

Table IV. In a bulk material, the coefficient of isothermal compressibility can be represented as the inverse of the bulk modulus[70] and can be thought of as the relative volume change that will occur in response to an applied stress. From Fig. 2, one can see good agreement between the AGNI platform and experiments. As described previously, the rate of change in the isothermal compressibility can be calculated by assuming a linear rate of change. Experiments predict a rate of change of $4.17 \times 10^{-7} \frac{1}{\text{GPa K}}$, while EAM-A and AGNI yield rates of $5.67 \times 10^{-7} \frac{1}{\text{GPa K}}$ and $4.11 \times 10^{-7} \frac{1}{\text{GPa K}}$, respectively.

Figure 2 also provides information about the change in lattice parameter as a function of temperature. As shown in Fig. 2(b), AGNI and experimental values of the change in lattice parameter as a function of temperature show exceptional agreement over the entire temperature range. Small deviations close to the melting temperature can be explained from the results obtained in our previous work.[38] As before, if we take the slope of this curve, information about the rate of change in lattice parameter as a function of temperature can be calculated. Experiments indicate a rate of change of $9.33 \times 10^{-5} \frac{\text{Å}}{\text{K}}$, while AGNI predicts a rate of $1.16 \times 10^{-4} \frac{\text{Å}}{\text{K}}$.

Finally, the information encoded in the change in lattice parameter can be used to calculate the coefficient of linear expansion as a function of temperature.[71] A cubic spline is fit to the lattice parameter values, shown in black in Fig. 2(b). The derivative of this spline is then used to calculate the coefficient of linear expansion, shown in Fig. 2(c). As the difference in the lattice parameter between experiments and PBE creates an artificial shift in the coefficient of linear expansion, the values in Fig. 2(c) are referenced to the value at 100 K for both AGNI and experiments. As there are small deviations in the lattice parameter at high temperatures, errors in the coefficient of linear expansion, at these same temperatures, are to be expected. Even with small discrepancies near the melting temperature, the agreement between AGNI and experiments can clearly be seen.

IV. CONCLUSION

In this work, the AGNI ML scheme was used to simulate the dynamic behavior of platinum under various forms of strain. We employed MD simulations to simulate the stress–strain relationships, under those strains, to predict the temperature dependence of the elastic constants of platinum. From these constants, other properties such as the bulk, shear, and Young's modulus were also calculated as a function of temperature. MD simulations were also performed to obtain the temperature dependence of properties such as the lattice parameter, isothermal compressibility, and coefficient of linear expansion. The results obtained from these simulations were then compared against experimental values. A critical topic that must be addressed is the model's transferability to configuration spaces not included in its training set. While many of the configurations presented in this work are not explicitly contained in any of the three model's training data, they do share similarities to them, and therefore, the model can reasonably predict such environments. In contrast, the models used in this work cannot be used to make accurate predictions of surface regions as such domains are geometrically very different. However, as the ML models can be iteratively improved, unlike semi-empirical/classical potentials, this deficiency can be addressed by adding these poorly predicted configurations to each model's respective training set to improve their accuracy.

As the AGNI models presented in this work were trained on DFT data, using the PBE exchange–correlation functional, it is expected that the AGNI model will make predictions at the DFT level-of-theory. Therefore, one cannot directly compare the absolute values of experiments and AGNI just as one could not directly compare the results of experiments with DFT. However, qualitative trends can be compared, and from them, quantitative changes in these trends can also be calculated. Upon examination of these trends and their rates of change, AGNI shows excellent agreement with respect to experiments, outperforming all EAM potentials for platinum. Using ML to obtain high fidelity properties of materials, with accuracy greater than that of semi-empirical potentials, such as those considered in this work, at time and length scales far beyond those of QM methods, provides yet another layer of validation that these methodologies can, and should, be used to push the boundaries of nano-scale materials research.

DATA AVAILABILITY

The raw data required to reproduce these findings are available at https://khazana.gatech.edu. All ML models used in this work can be found at https://agni-web.herokuapp.com.

REFERENCES

[1]V. Botu, J. Chapman, and R. Ramprasad, "A study of adatom ripening on an Al (111) surface with machine learning force fields," Comput. Mater. Sci. **129**, 332–335 (2016).

[2]S. M. Rassoulinejad-Mousavi and Y. Zhang, "Interatomic potentials transferability for molecular simulations: A comparative study for platinum, gold and silver," Sci. Rep. **8**, 2424 (2018).

[3]G. Grochola, S. P. Russo, and I. K. Snook, "On fitting a gold embedded atom method potential using the force matching method," J. Chem. Phys. **123**, 204719 (2005).

[4]C. J. O'Brien, C. M. Barr, P. M. Price, K. Hattar, and S. M. Foiles, "Grain boundary phase transformations in ptau and relevance to thermal stabilization of bulk nanocrystalline metals," J. Mater. Sci. **53**, 2911–2927 (2018).

[5]X. W. Zhou, R. A. Johnson, and H. N. G. Wadley, "Misfit-energy-increasing dislocations in vapor-deposited CoFe/NiFe multilayers," Phys. Rev. B **60**, 144113 (2004).

[6]S. M. Foiles, M. I. Baskes, and M. S. Daw, "Embedded-atom-method functions for the fcc metals Cu, Ag, Au, Ni, Pd, Pt, and their alloys," Phys. Rev. B **59**, 11693 (1999).

[7]P. Hohenberg and W. Kohn, "Inhomogeneous electron gas," Phys. Rev. **136**, B864–B871 (1964).

[8]W. Kohn and L. J. Sham, "Self-consistent equations including exchange and correlation effects," Phys. Rev. **140**, A1133–A1138 (1965).

[9]R. O. Jones, "Density functional theory: Its origins, rise to prominence, and future," Rev. Mod. Phys. **87**, 897–923 (2015).

[10]J. E. Jones and S. Chapman, "On the determination of molecular fields," Proc. R. Soc. London, Ser. A **106**, 463–477 (1924).

[11]M. S. Daw and M. I. Baskes, "Embedded-atom method: Derivation and application to impurities, surfaces, and other defects in metals," Phys. Rev. B **29**, 6443–6453 (1984).

[12]M. S. Daw, S. M. Foiles, and M. I. Baskes, "The embedded-atom method: A review of theory and applications," Mater. Sci. Rep. **9**, 251–310 (1993).

[13]J. Tersoff, "New empirical approach for the structure and energy of covalent systems," Phys. Rev. B **37**, 6991–7000 (1998).

[14]M. Z. Bazant, E. Kaxiras, and J. F. Justo, "Environment-dependent interatomic potential for bulk silicon," Phys. Rev. B **56**, 8542–8552 (1997).

[15]A. C. T. van Duin, S. Dasgupta, F. Lorant, and W. A. Goddard, "ReaxFF: A reactive force field for hydrocarbons," J. Phys. Chem. A **105**, 9396–9409 (2001).

[16]A. R. Setoodeh and H. Attariani, "Nanoscale simulations of Bauschinger effects on a nickel nanowire," Mater. Lett. **62**, 4266–4268 (2008).

[17]D. Poulikakos, S. Arcidiacono, and S. Maruyama, "Molecular dynamics simulations in nanoscale heat transfer: A review," Micro. Thermophys. Eng. **7**, 181–206 (2003).

[18]B. Baretzky, M. Baró, G. Grabovetskaya, J. Gubicza, M. Ivanov, Y. Kolobov, T. Langdon, J. Lendvai, A. Lipnitskii, A. Mazilkin, A. Nazarov, J. Nogués, I. Ovidko, S. Protasova, G. Raab, Á. Révész, N. Skiba, M. Starink, B. Straumal, S. Suriñach, T. Ungár, and A. Zhilyaev, "Fundamentals of interface phenomena in advanced bulk nanoscale materials," Rev. Adv. Mater. Sci. **9**, 45–108 (2005).

[19]J. Chapman, R. Batra, B. P. Uberuaga, G. Pilania, and R. Ramprasad, "A comprehensive computational study of adatom diffusion on the aluminum (100) surface," Comput. Mater. Sci. **158**, 353–358 (2019).

[20]F. Bianchini, J. R. Kermode, and A. De Vita, "Modelling defects in Ni–Al with EAM and DFT calculations," Modell. Simul. Mater. Sci. Eng. **24**, 045012 (2016).

[21]J. Gasteiger and J. Zupan, "Neural networks in chemistry," Angew. Chem., Int. Ed. **32**, 503–527 (1993).

[22]B. G. Sumpter, C. Getino, and D. W. Noid, "Theory and applications of neural computing in chemical science," Annu. Rev. Phys. Chem. **45**, 439–481 (1994).

[23]K. Rajan, "Materials informatics," Mater. Today **8**, 38–45 (2005).

[24]R. Ramprasad, R. Batra, G. Pilania, A. Mannodi-Kanakkithodi, and C. Kim, "Machine learning and materials informatics: Recent applications and prospects," npj Comput. Mater. **3**, 54 (2017).

[25]A. Mannodi-Kanakkithodi, A. Chandrasekaran, C. Kim, T. D. Huan, G. Pilania, V. Botu, and R. Ramprasad, "Scoping the polymer genome: A roadmap for rational polymer dielectrics design and beyond," Mater. Today **21**, 785–796 (2017).

[26]C. Kim, A. Chandrasekaran, T. D. Huan, D. Das, and R. Ramprasad, "Polymer genome: A data-powered polymer informatics platform for property predictions," J. Phys. Chem. C **122**, 17575–17585 (2018).

[27]G. Pilania, C. Wang, X. Jiang, S. Rajasekaran, and R. Ramprasad, "Accelerating materials property predictions using machine learning," Sci. Rep. **3**, 2810 (2018).

[28]T. D. Huan, A. Mannodi-Kanakkithodi, and R. Ramprasad, "Accelerated materials property predictions and design using motif-based fingerprints," Phys. Rev. B **92**, 014106 (2015).

[29]A. Mannodi-Kanakkithodi, G. Pilania, T. D. Huan, T. Lookman, and R. Ramprasad, "Machine learning strategy for the accelerated design of polymer dielectrics," Sci. Rep. **6**, 20952 (2016).

[30]V. Botu and R. Ramprasad, "Adaptive machine learning framework to accelerate *ab initio* molecular dynamics," Int. J. Quantum Chem. **115**, 1074–1083 (2015).

[31]V. Botu and R. Ramprasad, "Learning scheme to predict atomic forces and accelerate materials simulations," Phys. Rev. B **92**, 094306 (2015).

[32]V. Botu, R. Batra, J. Chapman, and R. Ramprasad, "Machine learning force fields: Construction, validation, and outlook," J. Phys. Chem. C **121**, 511–522 (2017).

[33]T. D. Huan, R. Batra, J. Chapman, S. Krishnan, L. Chen, and R. Ramprasad, "A universal strategy for the creation of machine learning based atomistic force fields," npj Comput. Mater. **3**, 37 (2017).

[34]J. Behler and M. Parrinello, "Generalized neural-network representation of high- dimensional potential-energy surfaces," Phys. Rev. Lett. **98**, 146401 (2007).

[35]A. P. Bartók and G. Csányi, "Gaussian approximation potentials: A brief tutorial introduction," Int. J. Quantum Chem. **115**, 1051–1057 (2015).

[36]S. Chmiela, A. Tkatchenko, H. E. Sauceda, I. Poltavsky, K. T. Schütt, and K.-R. Müller, "Machine learning of accurate energy-conserving molecular force fields," Sci. Adv. **3**, e1603015 (2017).

[37]T. D. Huan, R. Batra, J. Chapman, C. Kim, A. Chandrasekaran, and R. Ramprasad, "Iterative-learning strategy for the development of application-specific atomistic force fields," J. Phys. Chem. C **123**, 20715 (2019).

[38]J. Chapman, R. Batra, and R. Ramprasad, "Machine learning models for the prediction of energy, forces, and stresses for platinum," Comput. Mater. Sci. **174**, 109483 (2020).

[39]C. Kim, A. Chandrasekaran, A. Jha, and R. Ramprasad, "Active-learning and materials design: The example of high glass transition temperature polymers," MRS Commun. **9**, 860–866 (2019).

[40]R. Liu, A. Kumar, Z. Chen, A. Agrawal, V. Sundararaghavan, and A. Choudhary, "A predictive machine learning approach for microstructure optimization and materials design," Sci. Rep. **5**, 11551 (2015).

[41]A. Mosavi, T. Rabczuk, and A. R. Varkonyi-Koczy, "Reviewing the novel machine learning tools for materials design," in *Recent Advances in Technology Research and Education*, edited by D. Luca, L. Sirghi, and C. Costin (Springer International Publishing, Cham, 2018), pp. 50–58.

[42]J. E. Saal, S. Kirklin, M. Aykol, B. Meredig, and C. Wolverton, "Materials design and discovery with high-throughput density functional theory: The open quantum materials database (OQMD)," JOM **65**, 1501–1509 (2013).

[43]R. Farraro and R. B. Mclellan, "Temperature dependence of the Young's modulus and shear modulus of pure nickel, platinum, and molybdenum," Metall. Trans. A **8**, 1563–1565 (1977).

[44]T. Hamada, S. Hitomi, Y. Ikematsu, and S. Nasu, "High-temperature creep of pure platinum," Mater. Trans., JIM **37**, 353–358 (1996).

[45]R. E. Macfarlane, J. A. Rayne, and C. K. Jones, "Anomalous temperature dependence of shear modulus C_{44} for platinum," Phys. Lett. **18**, 91–92 (1965).

[46]R. Huang, Y.-H. Wen, Z.-Z. Zhu, and S.-G. Sun, "Structure and stability of platinum nanocrystals: From low-index to high-index facets," J. Mater. Chem. **21**, 11578–11584 (2011).

[47]M. Taravillo, V. G. Baonza, J. E. F. Rubio, J. Núñez, and M. Cáceres, "The temperature dependence of the equation of state at high pressures revisited: A universal model for solids," J. Phys. Chem. Solids **63**, 1705–1715 (2002).

[48]A. Erba, J. Baima, I. Bush, R. Orlando, and R. Dovesi, "Large-scale condensed matter dft simulations: Performance and capabilities of the crystal code," J. Chem. Theory Comput. **13**, 5019–5027 (2017).

[49]J. Hafner, "*Ab-initio* simulations of materials using VASP: Density-functional theory and beyond," J. Comput. Chem. **29**, 2044–2078 (2008).

[50]D. H. Chung and W. R. Buessem, "The Voigt Reuss Hill approximation and elastic moduli of polycrystalline MgO, CaF_2, β-ZnS, ZnSe, and CdTe," J. Appl. Phys. **38**, 2535–2540 (1967).

[51]R. Batra, H. D. Tran, C. Kim, J. Chapman, L. Chen, A. Chandrasekaran, and R. Ramprasad, "General atomic neighborhood fingerprint for machine learning-based methods," J. Phys. Chem. C **123**, 15859–15866 (2019).

[52]G. Kresse and J. Furthmüller, "Efficient iterative schemes for *ab initio* total energy calculations using a plane-wave basis set," Phys. Rev. B **54**, 11169 (1996).

[53]G. Kresse and D. Joubert, "From ultrasoft pseudopotentials to the projector augmented wave method," Phys. Rev. B **59**, 1758 (1999).

[54]H. Jònsson, G. Mills, and K. W. Jacobsen, "Nudged elastic band method for finding minimum energy paths of transitions," Classical Quantum Dyn. Condens. Phase Simul. **50**, 385 (1998).

[55]H. Jònsson and G. Henkelman, "Improved tangent estimate in the nudged elastic band method for finding minimum energy paths and saddle points," J. Chem. Phys. **113**, 9978 (2000).

[56]H. Jònsson, G. Henkelman, and B. Uberuaga, "A climbing image nudged elastic band method for finding saddle points and minimum energy paths," J. Chem. Phys. **113**, 9901 (2000).

[57]J. P. Perdew, K. Burke, and Y. Wang, "Generalized gradient approximation for the exchange-correlation hole of a many electron system," Phys. Rev. B **54**, 16533 (1996).

[58]P. E. Blöchl, "Projector augmented wave method," Phys. Rev. B **50**, 17953 (1994).

[59]H. J. Monkhorst and J. D. Pack, "Special points for Brillouin-zone integrations," Phys. Rev. B **13**, 5188 (1976).

[60] A. Chandrasekaran, D. Kamal, R. Batra, C. Kim, L. Chen, and R. Ramprasad, "Solving the electronic structure problem with machine learning," npj Comput. Mater. **5**, 22 (2019).

[61] S. Plimpton, "Fast parallel algorithms for short-range molecular dynamics," J. Comput. Phys. **117**, 1–19 (1995).

[62] J. Byggmästar, A. Hamedani, K. Nordlund, and F. Djurabekova, "Machine-learning interatomic potential for radiation damage and defects in tungsten," Phys. Rev. B **100**, 144105 (2019).

[63] T. Sun, K. Umemoto, Z. Wu, J.-C. Zheng, and R. M. Wentzcovitch, "Lattice dynamics and thermal equation of state of platinum," Phys. Rev. B **78**, 024304 (2008).

[64] S. M. Collard and R. B. McLellan, "High-temperature elastic constants of platinum single crystals," Acta Metall. Mater. **40**, 699–702 (1992).

[65] J. J. Mortensen, K. Kaasbjerg, S. L. Frederiksen, J. K. Nørskov, J. P. Sethna, and K. W. Jacobsen, "Bayesian error estimation in density-functional theory," Phys. Rev. Lett. **95**, 216401 (2005).

[66] A. Stroppa and G. Kresse, "The shortcomings of semi-local and hybrid functionals: What we can learn from surface science studies," New J. Phys. **10**, 063020 (2008).

[67] J. E. Angelo and M. I. Baskes, "Interfacial studies using the EAM and MEAM," Interface Sci. **4**, 47–63 (1997).

[68] M. I. Baskes, S. M. Foiles, and M. S. Daw, "Application of the embedded atom method to the fracture of interfaces," J. Phys. Colloques **49**, C5-483–C5-495 (1988).

[69] W.-J. Ding, J.-X. Yi, P. Chen, D.-L. Li, L.-M. Peng, and B.-Y. Tang, "Elastic properties and electronic structures of typical Al–Ce structures from first-principles calculations," Solid State Sci. **14**, 555–561 (2012).

[70] J. L. Tallon and A. Wolfenden, "Temperature dependence of the elastic constants of aluminum," J. Phys. Chem. Solids **40**, 831–837 (1979).

[71] S. Zhang, H. Li, S. Zhou, and T. Pan, "Estimation thermal expansion coefficient from lattice energy for inorganic crystals," Jpn. J. Appl. Phys., Part 1 **45**, 8801–8804 (2006).